Scanning infrared radiometer for measuring the air–sea temperature difference

Joseph A. Shaw, Domenico Cimini, Ed R. Westwater, Yong Han, Heather M. Zorn, and James H. Churnside

We describe a vertically scanning infrared radiometer for measuring the air–sea temperature difference without disturbing the water skin layer. The radiometer operates with a single wavelength channel that is 1.1 μm wide, centered on 14.2 μm, on the short-wavelength edge of a CO_2 atmospheric absorption band. The resulting high atmospheric absorption enables calibration of the horizontal-viewing signal with an *in situ* air-temperature sensor. The signal at all other scan angles is measured relative to that at the horizontal, providing a differential air–sea temperature measurement that is nearly independent of calibration offsets that can be a problem with independent air- and water-temperature sensors. We show data measured on a ship in the Tropical Western Pacific Ocean during July 1999, which exhibit important discrepancies from *in situ* data using bulk air- and water-temperature sensors. These discrepancies illustrate important differences between bulk versus skin water temperature. © 2001 Optical Society of America

OCIS codes: 010.0010, 120.0120, 120.5630, 120.0280.

1. Introduction

The ability to measure the air–water temperature difference is of great benefit to studies of the air–sea interface. Air–sea heat fluxes drive much of the energetics of the marine boundary layer, a key component of climate models.[1] The air–sea temperature difference also indicates stability, which helps determine the sea-surface roughness. For example, Shaw and Churnside[2] used laser-glint data to show that the sea-surface mean-square slope increases for a given wind speed when the air–sea temperature difference is negative, and Hwang and Shemdin[3] showed that sea-surface roughness decreases when it is positive. Therefore, the measurement of the air–sea interface stability is becoming an important part of retrieving near-surface wind vectors from microwave radiometer and radar data.[4,5]

Measurement of the air–sea temperature difference with *in situ* sensors is difficult because submerged temperature sensors measure the bulk water temperature, which can be quite different from the skin temperature.[6–8] The water skin temperature is most readily measured with a radiometer, but *in situ* sensors are also used. In either case, the subtraction of temperatures from separate air and water sensors is inevitably troublesome because each sensor has different calibration errors, and the air–sea temperature difference can be a small difference of two relatively large numbers.

A more reliable measurement is possible from differential radiometric techniques involving a single instrument that produces measurements either at different wavelengths or at different angles. For example, the Marine-Atmospheric Emitted Radiance Interferometer (M-AERI) has recently been used successfully to retrieve air–sea temperature differences from emission spectra measured at several different angles.[9] Another related technique is to measure sea-surface emission at two or more wavelengths having different optical depths in water to retrieve temperature profiles in the top layer of the water where the heat flow is dominated by molecular conductivity.[10–12] This layer is within approxi-

mately the top 0.2 mm, making mechanical temperature profiling extremely difficult at best, especially in this thin top layer of the open ocean.[13] Given a sufficiently small uncertainty ($\lesssim 0.01$ °C), multispectral radiometric measurements can yield an air–sea heat flux.

A relatively new, promising technique for measuring the air–sea temperature difference from a ship or other near-surface platform uses a vertically scanning radiometer operating on a spectral band with strong atmospheric absorption. The sea-surface skin temperature, corrected for atmospheric reflection, can be derived from the upward and downward views; and the air temperature can be derived from the horizontal view. The signal at other angles can also provide information on the vertical air-temperature profile either below or above the radiometer. A microwave radiometer based on this principle operates on the 5-mm O_2 absorption band,[14–17] and now we have developed a vertically scanning infrared radiometer that uses the same principle to determine the air–sea temperature difference from radiometric measurements on the 14-μm CO_2 absorption band. In this paper we describe this radiometer, its calibration, and data measured by it in the Tropical Western Pacific Ocean during the Nauru99 cruise.[17,18]

2. Radiometer System

The basic concept of this radiometer is the measurement of atmospheric and oceanic emissions at a spectral band that has relatively high atmospheric absorption from a uniformly mixed gas. Our infrared radiometer operates on the edge of a CO_2 absorption band, so changes in the horizontal radiance indicate local air-temperature changes at the instrument height, as long as we avoid operating in the vicinity of a CO_2 source (such as engine exhaust). The optical bandwidth is chosen to provide atmospheric absorption that is high enough to yield an accurate local air-temperature measurement at the horizontal scan direction, while being low enough that the radiometer can still see the sea-surface emission from the deployment height.

We designed the radiometer with the primary goal of deployment on a ship, approximately 10 m above the water. It was to be mounted on a boom extending over the water (see Section 5), with periodic access to fill the detector Dewar with liquid nitrogen, clean the optics, and perform calibrations. It had to be able to survive extended deployment in a sea-salt environment, possibly with direct sea spray because it would be mounted near the bow of the ship to observe relatively undisturbed water.

Figure 1 illustrates the scanning infrared air–sea radiometer optical system, which includes a vertical-plane scan mirror, an objective lens in a protective housing, an optical bandpass filter, and a HgCdTe detector operating in photovoltaic mode in a liquid-nitrogen-cooled vacuum Dewar. Only standard, off-the-shelf components were used for this radiometer prototype, although the detector vendor selected
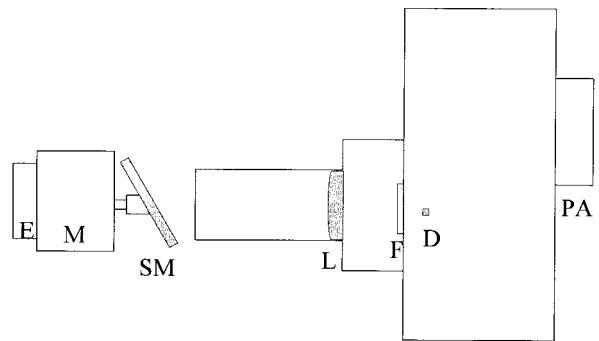

Fig. 1. Schematic layout of the scanning infrared radiometer. E is the angle encoder, M is the scan mirror stepper motor, SM is the scan mirror, L is the objective lens, F is the optical filter, D is the detector inside a liquid-nitrogen Dewar, and PA is the preamplifier. The signal from the preamplifier is digitized and processed by a computer.

chips that would maximize photovoltaic responsivity at the 14-μm spectral band and tuned the preamplifier to provide optimal performance in the 2–3-Hz frequency range. We chose to use the ac-coupled detector in photovoltaic mode to minimize the noise that otherwise arises when an infrared detector is modulated at such low frequencies. The detector has a peak normalized detectivity D^* (at 1-kHz modulation with 1-Hz noise bandwidth) of 3.5×10^{-11} cm $Hz^{1/2}$/W near 13 μm. Its response is approximately 80% or more of peak throughout the radiometer bandwidth.

The 50-cm-diameter gold-coated scan mirror mounts on the shaft of a stepper motor that rotates continuously during operation. A stepper motor is used because it allows the computer to reliably keep track of the scan mirror angular position. The motor spins the scan mirror in a vertical plane that is orthogonal to the radiometer's optical axis. Thus the radiometer field of view is unobstructed for all but a small portion where the beam crosses the plate on which the radiometer components are mounted. The current system uses a variable scan rate that is usually approximately two rotations per second. The mechanically scanning mirror is the only modulation mechanism.

The lens is a 25.4-mm-diameter f/2.5 plano–convex singlet made of ZnSe and is antireflection coated to achieve greater than 90% transmissivity over the radiometer bandwidth. A protective barrel serves as the lens mount and optical baffle, and it helps protect the lens from sea spray. The lens, mounted near the midpoint of this barrel, acts as the radiometer's aperture stop, and the 1-mm-diameter detector acts as the field stop, resulting in a 0.9° full-angle field of view. For a radiometer height of 10 m and this field of view, the horizontal radiometer view does not intersect the sea surface for over 1.2 km, approximately ten times farther than the band-averaged atmospheric penetration depth for the radiometer.

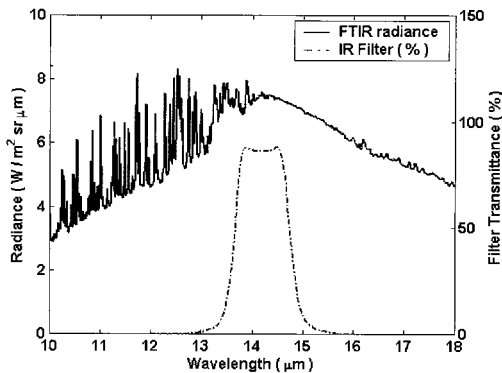A bandpass interference filter behind the lens pro-

Fig. 2. Scanning radiometer filter response function (in percent), plotted with a Fourier-transform infrared (FTIR) measurement of downwelling atmospheric spectral radiance in the same spectral region. The relatively smooth radiance curve between approximately 14.0 and 15.9 μm is the highly absorbing CO_2 band. At shorter wavelengths, the atmosphere becomes more transmissive, and the spectrum shows absorption features of atmospheric water vapor and other gases.

Fig. 3. Atmospheric penetration depth (distance for which the optical depth is 1 and the transmissivity is equal to e^{-1}) versus wavelength within the radiometer filter half-power bandwidth.

vides a spectral bandwidth centered at 14.20 μm with half-power points of 13.63 and 14.76 μm. The filter response is in the range of 85–88% between wavelengths of 13.8 and 14.6 μm. Radiative transfer calculations originally called for a narrower bandpass centered at a shorter wavelength to match the atmospheric optical depth of our 5-mm wavelength radiometer,[14–16] but the present bandwidth was the closest we could obtain with a standard commercial filter.

Figure 2 shows the filter response function and a downwelling atmospheric emission spectrum we measured near Nauru Island, both plotted versus wavelength. The zenith downwelling atmospheric radiance spectrum matches a blackbody curve at the local air temperature near the center of the CO_2 absorption band at 14.97 μm and remains highly opaque down to approximately 14.3 μm. Below this, there is increasing atmospheric penetration of the radiometer beam until the filter response falls off near 13.5 μm. Thus the long-wave end of the filter bandwidth sees primarily the air immediately in front of the radiometer, and the shortwave end provides most of the scan-angle-dependent radiance.

Figure 3 shows the atmospheric penetration depth for a horizontal path in a tropical atmosphere model[19] plotted versus wavelength within the half-power bandwidth of the filter (penetration depth is the distance in the atmosphere for which the optical depth is 1 and for which the incident radiation is reduced to e^{-1} times its original value). The band-averaged atmospheric penetration depth (weighted by the filter bandwidth) is 150 m. The spectral penetration depth for this filter is approximately 400 m near the short-wave half-power point (13.6 μm), 50 m near band center (14.2 μm), and less than 10 m near the long-wave half-power point (14.7 μm). The maximum penetration is approximately 800 m near 13.8
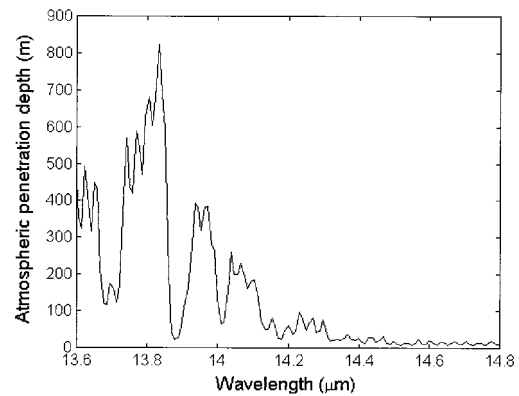
μm. A custom filter could provide a more desirable bandpass, but at higher cost.

The skin depth of the ocean for this infrared bandwidth is only 3 μm, or slightly more than one fifth of the optical wavelength. Figure 4 shows the ocean skin depth d calculated for the infrared spectral range of 3–15 μm from[20]

$$d = \frac{c}{2\omega k},\qquad(1)$$

where c is the speed of light, ω is the optical radian frequency, and k is the imaginary component of the complex refractive index for water.[21] Note in Fig. 4 that the water penetration depth near the 4.3-μm CO_2 absorption band is at least an order of magnitude higher than at the 15-μm CO_2 band. Therefore a similar radiometer could operate at this short-wavelength band and see deeper into the sea-surface skin layer. In fact, at a 5-mm wavelength, our scanning microwave radiometer sees an ocean penetration depth of approximately 300 μm (0.3 mm)[14] or 2
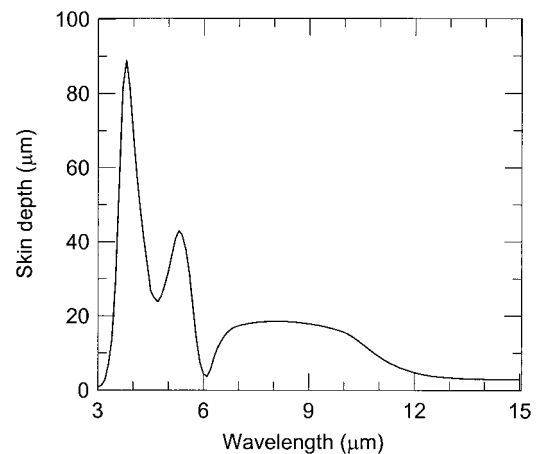

Fig. 4. Skin depth of water versus wavelength. The scanning infrared radiometer operates in the spectral range 13.63–14.76 μm where the skin depth is approximately 3 μm.

full orders of magnitude deeper than that seen by the long-wave infrared radiometer.

3. Calibration

Relative measurement of the air and water skin temperatures is the key to the robustness of the scanning infrared air–sea radiometer. Calibration offsets do not affect the air–sea temperature difference, which requires one to know only the radiometer gain, which tells how much the output voltage changes for a given change in input radiance or brightness temperature. We derive the air–sea temperature difference from the difference in radiometer voltages at the horizontal and downlooking scan angles. The resulting temperature difference is nearly independent of the radiometer offset, which enables more robust retrieval of small temperature differences than is possible when the outputs of two independent sensors are subtracted.

We follow the standard procedure of calibrating the radiometer in terms of an offset and gain, which are the zero intercept and slope of a linear fit between the radiometer output voltage and the input radiance, as indicated in Eq. (2):

$$L(\theta) = L_0 + GV(\theta), \qquad (2)$$

where $L(\theta)$ is the measured radiance as a function of scan angle θ, L_0 is the offset radiance (signal measured by the radiometer in the absence of input, arising from optics self-emission, and so on), G is the radiometer gain, and $V(\theta)$ is the scan-angle-dependent radiometer output voltage. Calibration of the radiometer gain requires two calibration points, preferably covering the range of expected radiances or brightness temperatures. However, the usual approach of viewing two high-quality blackbody sources is not practical in this case because the radiometer is designed to operate from a boom extended out over the ocean, with the computer and associated electronics housed in a protective trailer on the deck of the ship. Even in calm seas, a blackbody surface could be ruined in a short period of time by sea salt. Furthermore, the cables connecting the blackbody optical head and electronic controller would be excessively long if the optical head were deployed with the radiometer while the controller remained in the trailer. For these reasons, we chose to calibrate the radiometer gain in the laboratory and then, during deployment, periodically check it with a blackbody source when the radiometer was brought in several times each day to fill the liquid-nitrogen Dewar.

During deployment, we provided one reference calibration point during each scan by relating the horizontally viewing radiometer voltage to the local air temperature measured with a high-quality air-temperature sensor that mounts next to the radiometer (Vaisala, HMP 233). This calibration technique is as precise as the air-temperature sensor reading if the atmosphere is uniform over a horizontal distance of approximately 150 m. The calibration does not depend on the absolute accuracy of the air-temperature sensor because we retrieve only a temperature difference from the corresponding radiometer voltage changes between the horizontal and nadir views.

Prior to deployment, we measured the radiometer gain for multiple hours by continuously scanning across two blackbody calibration sources. We found that the gain drifted slowly enough that a second calibration point once every several hours provides sufficient calibration. However, as described in Section 5, this plan was foiled in our tropical ship deployment by the presence of strong temperature gradients near the radiometer, caused largely by solar heating of the ship's deck. The result was that only nighttime calibrations on the ship were useful, and some of those were questionable.

Fortunately we had several other options for vicarious calibration of the scanning infrared air–sea radiometer during its ocean deployment. On the same ship we had a Fourier-transform infrared (FTIR) spectroradiometer that we routinely used for high-accuracy measurements of atmospheric emission spectra.[22,23] In postprocessing we calibrated the scanning infrared radiometer data by using the usual air-temperature measurement at the radiometer as one calibration source and the FTIR measurement of zenith atmospheric emission as the second calibration source. We averaged the FTIR atmospheric emission spectra over the optical bandwidth of the radiometer to derive an equivalent radiance for the vertical radiometer view; and we averaged the Planck function, evaluated at the local air temperature, over the radiometer bandwidth to derive an equivalent radiance for the horizontal radiometer view. We then calculated the radiometer gain as the change in output voltage over the change in radiance. We calibrated in terms of radiance, with which the radiometer signal varies linearly, but then computed an equivalent brightness-temperature gain so that we could express our results in the more physically intuitive units of temperature.

Using the FTIR spectra to calibrate the scanning radiometer zenith data required us to identify clear versus cloudy periods. The short-wavelength end of the scanning radiometer filter response enables the radiometer to see higher into the atmosphere than desired, resulting in zenith signal variations when low clouds pass overhead. This would not be a problem except that the FTIR and scanning radiometer have different data-averaging times, beam widths ($0.9°$ for the scanning infrared, $2°$ for the FTIR), and locations (approximately 40 m apart). However, we were able to identify cloudy periods from the temporal variability of FTIR data and from a laser ceilometer and a millimeter-wave cloud radar operated by the National Oceanic and Atmospheric Administration (NOAA) Environmental Technology Laboratory (ETL) aboard the same ship. We calibrated the data shown here using FTIR data from clear periods, during which the overall calibration uncertainty of the

scanning air–sea temperature radiometer is estimated to be less than 0.2 K.

We also used other methods for providing a second postprocessing calibration point for the scanning infrared radiometer. For example, we retrieved air-temperature profiles above the ship from the 5-mm radiometer data[15–17] and then used the resulting profile in a radiative transfer program to compute the infrared atmospheric emission spectrum. By averaging this computed spectrum over the scanning infrared radiometer filter bandpass, we could arrive at an integrated atmospheric radiance that served as the second calibration point. Of course this approach is more uncertain than the direct use of measured FTIR spectra, but the results of the two calibration techniques agreed surprisingly well. The data shown in Section 5, however, were all calibrated with measured FTIR spectra to ensure that the data from the two scanning radiometers were as independent as possible. For future deployments, this scanning air–sea radiometer will be modified to include at least one integral calibration source.

4. Air–Sea Temperature Difference Retrieval

The calibration procedure described above results in a band-averaged radiance value at each radiometer scan angle. We retrieve the air–sea temperature difference from the difference between the horizontal and the nadir radiometer measurements, each averaged over an angular bin of approximately 5°. However, whereas the horizontal brightness temperature is given directly by the *in situ* air-temperature measurement, the nadir sea-surface brightness temperature is retrieved iteratively from the nadir radiance measurement.

The iterative retrieval of sea-surface temperature minimizes the difference between measured and modeled radiance, where the model considers emission from the sea surface, emission from the intervening atmosphere, and absorption by the intervening atmosphere, all weighted by the spectral response of the radiometer. First, a band-averaged radiance is calculated from the Planck function for an assumed value of sea-surface skin temperature, multiplied by the radiometer spectral response function, and integrated over wavelength. This modeled sea-surface radiance value is combined with atmospheric absorption and emission in a radiative transfer model and compared with the measured band-averaged radiance. Repeated iterations with appropriate adjustments to the initial temperature rapidly yield the sea-surface temperature. For a deployment height of 10 m, we assume constant temperature from the radiometer down to the sea surface. We verified with radiative transfer modeling that air-temperature gradients in the bottom 10 m produce a negligible effect on the nadir measurement, but may be important for downward angles away from nadir.

At each angle near nadir, the measured radiance L is modeled as

$$L = \int \{\varepsilon_s(\lambda) L_{bb}(\lambda, T_s)\tau(\lambda) + L_a(\lambda)$$
$$+ [1 - \varepsilon_s(\lambda)]L_{ra}(\lambda)\tau(\lambda)\} f(\lambda)d\lambda, \qquad (3)$$

where ε_s is the sea-surface emissivity; $L_{bb}(T_s)$ is the blackbody spectral radiance ($Wm^{-2}\, sr^{-1}\, \mu m^{-1}$) from the Planck function evaluated at the sea-surface temperature T_s; τ is the transmittance of the atmospheric path at the appropriate angle; L_a is the radiance emitted by the atmosphere between the radiometer and the sea surface; L_{ra} is the reflected atmospheric radiance; λ is the optical wavelength; and $f(\lambda)$ is the radiometer spectral response function. In the retrieval, we actually replace the wavelength-dependent atmospheric transmittance $\tau(\lambda)$ with a band-averaged value and remove it from the integral, then solve for a band-averaged version of the sea-surface emission term $L_{bb}(\lambda, T_s)$.

We calculated the sea-surface emissivity as an integral over a wind-roughened ensemble of specular facets using the isotropic, first-order Gaussian wave-slope probability density function of Cox and Munk[24] and a constant wind speed value of 5 m s^{-1} (the average wind speed for the period considered here). Because of the small range of nadir angles included in the sea-surface temperature retrieval, the effective rough-surface emissivity is nearly the same as the smooth-surface value given as one minus the unpolarized Fresnel reflectivity.[25] In our retrieval model we use the complex refractive-index values published by Hale and Querry for seawater.[21]

5. Measurements in the Tropical Pacific

In June and July 1999, we deployed the prototype scanning infrared air–sea temperature difference radiometer on the NOAA research vessel Ronald H. Brown (RHB) for a one-month cruise to study air–sea interaction and the effect of the island on the Atmospheric Radiation and Clouds Station operated on Nauru Island (0° latitude, 166° E longitude) in the Tropical Western Pacific Ocean for the U.S. Department of Energy's Atmospheric Radiation Measurement (ARM) program.[18] We loaded a suite of remote sensing instruments on the 83.5-m-long RHB in Darwin, Australia, during 10–15 June 1999. The ship then transited around Papua New Guinea up to Nauru Island, taking a position near there on 23 June 1999. The remaining time until 15 July was spent at various distances from the island, holding stationary or transiting around the island. In this paper we report data from the air–sea temperature difference radiometer collected during a period when the ship was in a stationary position approximately 1 km west of the island. During the example period discussed here, the wind speed varied between 4 and 6 m s^{-1}.

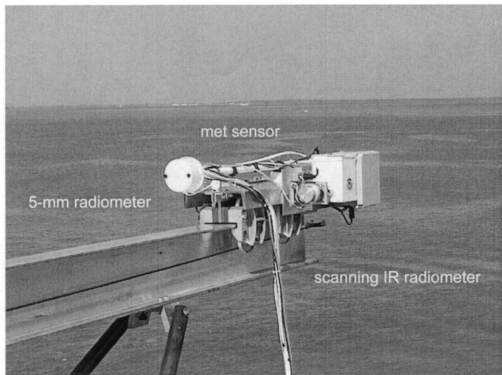The scanning infrared radiometer was deployed next to a scanning microwave radiometer that oper-

Fig. 5. Photograph of the scanning radiometer package deployed on the NOAA research vessel RHB in the South Pacific during June–July 1999. The scanning infrared radiometer is visible in the front, a scanning microwave radiometer is on the backside of the trolley, and the *in situ* temperature probe (met sensor) is on the top. The trolley moves back and forth along the boom, which is mounted on the roof of a sea container on the forward deck of the ship. The boom extends approximately 5 m beyond the port side of the ship.

Fig. 6. Uncalibrated radiometer signal versus scanning angle averaged over 6 min.

ates on the 5-mm O_2 absorption band.[14–17] The two scanning radiometers were mounted along with the Vaisala temperature and humidity probe on a boom that extended approximately 5 m beyond the port side of the RHB. The mean height above sea level of the radiometers on the boom was 10 m. A typical roll angle of 5° causes the mean height to vary by approximately ±0.44 m (4.4%), which can be ignored because radiative transfer simulations show that a change in the radiometer height by 1 m changes the retrieved air–sea temperature difference by less than 0.01 °C. Figure 5 is a photograph of the radiometers mounted on a trolley at the end of the boom, which was mounted on the roof of a mobile laboratory built from a standard sea container. The trolley enabled the entire radiometer package to be brought in to the roof of the sea container where an operator could fill the liquid-nitrogen Dewar, clean the mirrors, and run a full radiometer calibration with the temperature probe and an auxiliary blackbody source.

The plan to calibrate the scanning infrared radiometer periodically on top of the sea container was made impractical by extreme temperature gradients in the air above the sea container, caused by strong solar heating during the day. Therefore we relied primarily on postexperiment calibration using the *in situ* temperature probe for the horizontal view and downwelling atmospheric emission spectra measured with our FTIR spectroradiometer for the zenith view.

Other than these calibration difficulties, the boom-and-trolley configuration was a success: It usually kept the scanning radiometers above undisturbed water and also provided easy and convenient access to the instruments when needed. The boom mounting allowed us to avoid the difficulty of retrieving sea-surface temperatures from large angles away from nadir, where the sky reflection is larger and the surface emissivity uncertainties are more significant.
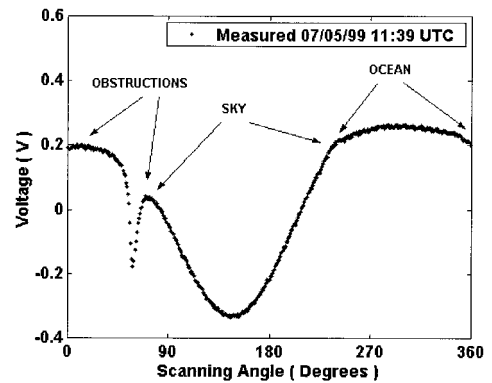
During periods of transit through heavy seas, the radiometers were locked in position on the sea container roof and covered for protection from the heavy spray that sometimes covered the entire bow. The optics were well protected throughout the experiment, with only the scanning mirror requiring cleaning no more than once daily.

Figure 6 is a plot of the raw radiometer signal before angle or radiometric calibration, showing the location of the ocean, atmosphere, and obstructions in the scan. An absolute angle encoder on the scan mirror motor shaft kept track of the relative angle, but sometimes it gave noisy data that made absolute angle calibration difficult. We eventually used a curve-fit algorithm to locate the zenith as the minimum point on the sky portion of the scan and set the angle there to 90°. An added advantage of this approach is that it always identifies the true zenith, regardless of ship pitch angle, and identifies the true horizon as 90° away from that point. Therefore the pitch of the ship does not change our readings to any measurable degree.

Figure 7 illustrates the radiometer signal after the angle calibration as described above and the radiometric calibration with the *in situ* temperature probe and the FTIR spectrum. The relative radiometer voltage was converted to a brightness-temperature dif-
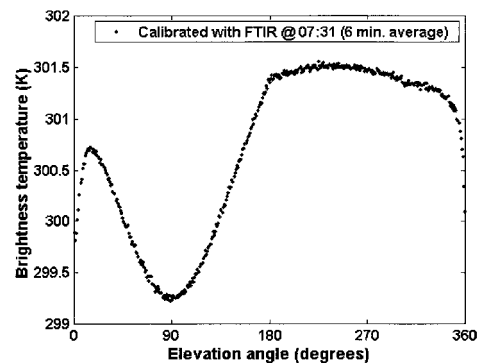

Fig. 7. Six-minute average of the radiometer signal in units of brightness temperature versus scan angle after angle and radiometric calibrations.
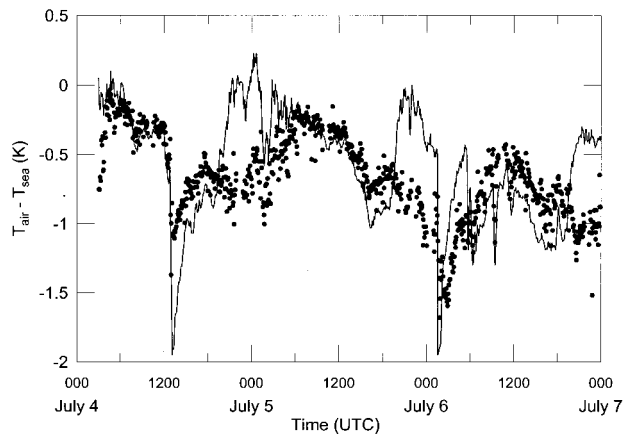
Fig. 8. Retrieved air–sea temperature differences from the scanning infrared radiometer (filled circles) and *in situ* air- and water-temperature sensors (solid curve) for 4–6 July 1999, near Nauru Island.

Fig. 9. Solar irradiance, wind speed, and wind direction for the three-day period shown in Fig. 8.

ference, as described in Section 3, and is shown as a 6-min average plotted versus the scan angle. The zero scan angle corresponds to the horizontal view toward the boom, where the beam is fully blocked by the metal plate on which the radiometer is mounted. The zenith sky is at 90°, around which the atmospheric emission is symmetric unless the atmospheric temperature itself is asymmetric. (Except in cases of extreme low-level temperature inversions, the minimum signal will always be at zenith.) The transition from the clear atmosphere to the ocean occurs at 180°, after which the radiometer sees the sea surface until the beam is blocked by the boom and radiometer mount from approximately 320° to 20°. Note that the signal near 360° (or 0°) is low because the aluminum mounting plate is angled slightly upward and reflects the atmosphere into the radiometer beam.

Figure 8 shows air–sea temperature differences retrieved from the scanning infrared radiometer with 5-min averages (filled circles) and from *in situ* measurements (solid curve) of the air temperature at a 15-m height (measured on a mast on the RHB bow) and the water temperature at a 5-cm depth from the RHB during 4–6 July 1999, with the ship sitting stationary less than 1 km west of Nauru Island (0°, 166° E). Note that our bulk measurements of the air–sea temperature difference are not exactly the same quantity as the operational bulk air–sea temperature difference because we use the water temperature at a 5-cm depth instead of the usual 5-m depth at the ship intake. However, during the three-day period shown here, the bulk water temperatures at 5-m and 5-cm depths agree within approximately 0.1 °C. Therefore our bulk air–sea temperature difference is not drastically different from the operationally defined bulk quantity.

Figures 8 and 9 show data starting and ending at Julian days 185 and 188, corresponding to local noon on 4 and 7 July 1999, respectively; local midnight occurs at 1200 UTC on each day. Figure 9 shows the
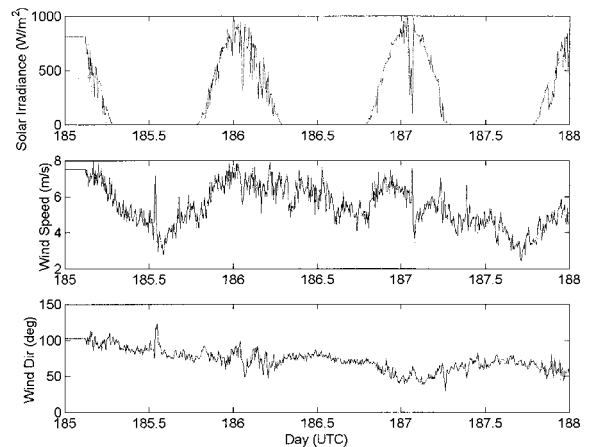
corresponding time series of solar irradiance, wind speed, and wind direction. There is a significant diurnal variation in the agreement between the bulk and the radiometric air–sea temperature difference data, with generally worse agreement during the day. The correlation coefficients for the radiometric and bulk data are 0.63 during the day (1900–0700 UTC) and 0.94 at night (0700–1900 UTC). Furthermore, the radiometer generally measured larger (more negative) air–sea temperature differences than the bulk sensors during the day and somewhat smaller differences during the night. We interpret these differences as a daytime warm layer and nighttime cool skin on the water.[7,8]

The majority of the structure in Fig. 8 is caused by changes in the air temperature, but it is also important to consider differences in the skin and bulk water temperatures. The important concept driving much of the subsequent discussion is that the water skin temperature follows the fluctuating air temperature more closely than does the bulk water temperature. During the daytime, the Sun warms the skin layer of the water while leaving the bulk water temperature essentially unchanged. Therefore the radiometric air–sea temperature difference tends to be more negative in the daytime than the bulk difference. Solar heating of the bulk air-temperature sensor can produce an artificially small air–sea temperature difference, which would increase the apparent discrepancy between the daytime bulk and the radiometric measurements. We see this kind of warm-layer effect each day (~1900–0700 UTC), with a clear correlation between the magnitude of the warm layer and cloud-induced fluctuations in the incident solar irradiance (top graph, Fig. 9).

At nighttime, the water skin temperature experiences evaporative cooling, allowing it to track slightly closer to the air temperature than does the bulk water temperature (which remains largely unaffected). The result is the development of a cool skin layer that produces an air–sea temperature difference that is usually 0.1–0.3 °C smaller than for the bulk temper-

atures.[7,8] The data in Fig. 8 show a cool skin effect occurring each night (~0700–1900 UTC), especially on 6 July when the wind speed is lower.

There are two relatively large downward spikes in the bulk air–sea temperature difference, near 1300 UTC on 4 July and 0200 UTC on 6 July. We attribute the first of these to a shift of wind direction (see bottom graph, Fig. 9), which briefly brought slightly cooler open-ocean air across the ship before the wind returned to blowing from the island to the ship (the island was due east of the ship during this entire three-day measurement period). The second spike appears during a short period of thick clouds (see top graph, Fig. 9), which allowed the air temperature to cool briefly. The scanning infrared radiometer observed both of these spikes, but with a smaller magnitude than the bulk sensors, particularly for the first (4 July) one. We believe that this is because the radiometer integrates its horizontal measurement across an average path length of 150 m (shorter for the long-wave end and longer for the shortwave end of the radiometer bandwidth). The horizontal radiometer measurement was directed toward the island, meaning that it was likely looking through the small burst of cool air into warmer air blowing from off the island. The second spike apparently was the result of air cooling over a larger area, resulting in better agreement between the radiometric and the bulk measurements.

The radiometric air–sea temperature difference data should be analyzed on space and time scales consistent with this integration path length in the atmosphere. Hence the minimum averaging time should be equal to the time it takes for the wind to blow along the radiometer integration path length. For a wind speed of 5 m s^{-1}, this implies a minimum averaging time of approximately 30 s. We have shown 5-min averages here, well outside of this minimum, but short enough to illustrate the capability of the radiometer to observe temperature changes of reasonably short duration.

The discrepancies between radiometric and bulk measurements of the air–sea temperature difference shown in Fig. 8 illustrate the importance of radiometric techniques to validate satellite sea-surface temperature data and to study air–sea interactions. Bulk temperature measurements miss much of the important dynamics of energy exchange, which occur almost exclusively in the skin layer on the water. Bulk data also can suffer from localized heating of ship-mounted air-temperature sensors.

The 5-mm microwave radiometer measurements are quite similar with the infrared data shown here, indicating similar day–night variability when compared with the bulk sensor data[26] (a detailed comparison of the data from the two radiometers and bulk sensors will appear in a later paper). We also note that the atmospheric portion of the scan from both scanning radiometers can be used to retrieve low-altitude atmospheric temperature profiles.[15–17]

The primary source of uncertainty in the retrieved air–sea temperature difference is from the radiome-ter gain calibration. Because the measured temperatures are so near the calibration temperatures, and because of the differential measurement, the offset is not particularly critical. However, changes in the gain affect the retrieved temperature difference directly, so our plans to add integral calibration sources should yield significant improvements to the long-term reliability of the radiometer. An improved angle encoder will make data processing somewhat easier, but will not significantly improve the data quality because simulations have shown that the retrieved air–sea temperature difference changes by only ±0.03 °C for each 0.9° of angular pointing error. The current approach of setting the angle of the minimum radiometer signal equal to the zenith appears to be as good as could be expected with any angle encoder, plus it offers the advantage of directly removing the signal dependence on ship pitch angle.

6. Summary and Conclusions

Vertically scanning radiometers operating on absorption bands of uniformly mixed atmospheric gases provide a potentially robust method to measure air–sea temperature differences without disturbing either the sea-surface skin layer or the air. The new scanning infrared radiometer that we have described operates on the short-wavelength edge of the 15-μm CO_2 absorption band and has successfully measured the air–sea temperature difference from a ship at sea. These data disagree with data from bulk sensors in an explainable and important fashion, showing daytime warm layers and nighttime cool skins. We are in the process of improving this radiometer by installing a heated calibration target for routine calibration of each scan and by installing an improved angle encoder on the scan mirror. We are also investigating options for a more ideal filter. These improvements will make this instrument more robust and easier to use. In the future we intend to exploit the different skin depths of scanning microwave and infrared radiometers to investigate air-temperature profiles and heat fluxes at both air–sea and air–snow interfaces.

References

1. J. W. Hurrell and K. E. Trenberth, "Global sea surface temperature analyses: multiple problems and their implications for climate analysis, modeling, and reanalysis," Bull. Am. Meteorol. Soc. **80,** 2661–2678 (1999).

2. J. A. Shaw and J. H. Churnside, "Scanning-laser glint measurements of sea-surface slope statistics," Appl. Opt. **36,** 4202–4213 (1997).

3. P. A. Hwang and O. H. Shemdin, "The dependence of sea surface slope on atmospheric stability and swell conditions," J. Geophys. Res. **93,** 13903–13912 (1988).

4. M. N. Pospelov, "Surface wind speed retrieval using passive microwave polarimetry: the dependence on atmospheric stability," IEEE Trans. Geosci. Remote Sens. **34,** 1166–1171 (1996).

5. W. C. Keller, W. J. Plant, and D. E. Weissman, "The dependence of X-band microwave sea return on atmospheric stability and sea state," J. Geophys. Res. **90,** 1019–1029 (1985).

6. P. Schluessel, W. J. Emery, H. Grassl, and T. Mammen, "On the bulk-skin temperature difference and its impact on satellite remote sensing of sea surface temperature," J. Geophys. Res. **95,** 13341–13356 (1990).

7. G. A. Wick, W. J. Emery, L. H. Kantha, and R. Schluessel, "The behavior of the bulk-skin sea surface temperature difference under varying wind speed and heat flux," J. Phys. Oceanogr. **26,** 1969–1988 (1996).

8. C. W. Fairall, E. F. Bradley, J. S. Godfrey, G. A. Wick, J. B. Edson, and G. S. Young, "Cool-skin and warm-layer effects on sea surface temperature," J. Geophys. Res. **101,** 1295–1308 (1996).

9. P. J. Minnett, R. O. Knuteson, F. A. Best, B. J. Osborne, J. A. Hanafin, and O. B. Brown, "The Marine-Atmospheric Emitted Radiance Interferometer: a high-accuracy, seagoing infrared spectroradiometer," J. Atmos. Oceanic Technol. **18,** 994–1013 (2001).

10. E. D. McAlister and W. McLeish, "A radiometric system for airborne measurement of the total heat flow from the sea," Appl. Opt. **9,** 2697–2705 (1970).

11. E. D. McAlister and W. McLeish, "Airborne measurements of the total heat flux from the sea during Bomex," J. Geophys. Res. **76,** 4172–4180 (1971).

12. W. McKeown, F. Bretherton, H. L. Huang, W. L. Smith, and H. E. Revercomb, "Sounding the skin of water: sensing air–water interface temperature gradients with interferometry," J. Atmos. Oceanic Technol. **12,** 1313–1327 (1995).

13. T. C. Mammen and N. von Bosse, "STEP—a temperature profiler for measuring the oceanic thermal boundary layer at the ocean-air interface," J. Atmos. Oceanic Technol. **7,** 312–322 (1990).

14. Y. G. Trokhimovski, E. R. Westwater, Y. Han, and V. Y. Leuski, "Air and sea surface temperature measurements using a 60-GHz microwave rotating radiometer," IEEE Trans. Geosci. Remote Sens. **36,** 3–15 (1998).

15. E. R. Westwater, Y. Han, V. G. Irisov, and V. Y. Leuskiy, "Sea–air and boundary layer temperatures measured by a scanning 5-mm wavelength radiometer: recent results," Radio Sci. **33,** 291–302 (1998).

16. E. R. Westwater, Y. Han, V. G. Irisov, V. Y. Leuskiy, E. N. Kadygrov, and S. A. Viazankin, "Remote sensing of boundary layer temperature profiles by a scanning 5-mm microwave radiometer and RASS: comparison experiments," J. Atmos. Oceanic Technol. **16,** 805–818 (1999).

17. J. A. Shaw, D. Cimini, E. R. Westwater, Y. Han, H. Zorn, and J. H. Churnside, "Air–sea temperature differences measured with scanning radiometers during Nauru99," in *Proceedings of the International Geoscience and Remote Sensing Symposium 2000* (Institute of Electrical and Electronics Engineers, New York, 2000), pp. 111–113.

18. M. J. Post and C. W. Fairall, "Early results from the Nauru99 campaign on NOAA ship Ronald H. Brown," in *Proceedings of the International Geoscience and Remote Sensing Symposium 2000* (Institute of Electrical and Electronics Engineers, New York, 2000), pp. 1151–1153.

19. G. P. Anderson, S. A. Clough, F. X. Kneizys, J. H. Chetwynd, and E. P. Shettle, "AFGL atmospheric constituent profiles (0–120 km)," Tech. Rep. AFGL-TR-86-0110 (NTIS AD A175173) (U.S. Air Force Geophysics Laboratory, Hanscom Air Force Base, Mass., 1986).

20. E. Hecht, *Optics*, 2nd ed. (Addison-Wesley, Reading, Mass., 1982), p. 110.

21. G. M. Hale and M. R. Querry, "Optical constants of water in the 200-nm to 200-μm wavelength region," Appl. Opt. **12,** 555–563 (1973).

22. J. A. Shaw, H. M. Zorn, J. J. Bates, and J. H. Churnside, "Observations of downwelling infrared spectral radiance at Mauna Loa, Hawaii during the 1997–1998 ENSO event," Geophys. Res. Lett. **26,** 1727–1730 (1999).

23. Y. Han, J. A. Shaw, J. H. Churnside, P. D. Brown, and S. A. Clough, "Infrared spectral radiance measurements in the tropical Pacific atmosphere," J. Geophys. Res. **102,** 4353–4356 (1997).

24. C. Cox and W. Munk, "Measurement of the roughness of the sea surface from photographs of the sun's glitter," J. Opt. Soc. Am. **44,** 838–850 (1954).

25. J. A. Shaw and C. Marston, "Polarized infrared emissivity for a rough water surface," Opt. Exp. **7,** 375–380 (2000), http://www.opticsexpress.org/oearchive/pdf/25342.pdf.

26. J. A. Shaw, D. Cimini, E. R. Westwater, and Y. Han, "Air-sea temperatures measured with scanning microwave and infrared radiometers in Nauru99," in *Proceedings of the Eleventh ARM Science Team Meeting* (U.S. Department of Energy, Washington, D.C., 2001), http://www.arm.gov/docs/documents/technical/conf_0103/index.html.